J-aggregation in indolenine dyes drives fluorescent crystals with large Stokes shifts and two-photon excited emission

Cell Reports
Physical Science

Article

J-aggregation in indolenine dyes drives fluorescent crystals with large Stokes shifts and two-photon excited emission

Graphical abstract

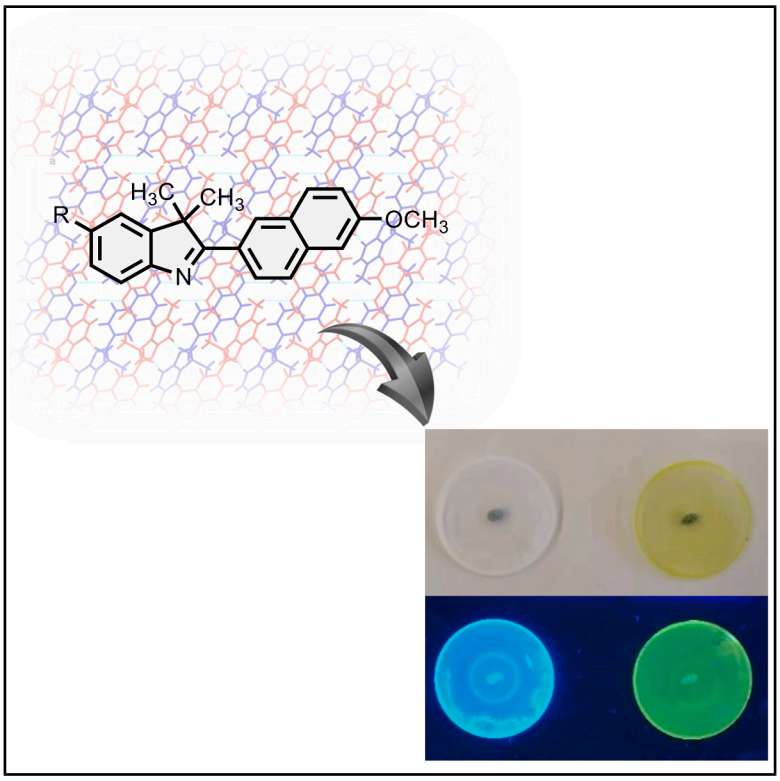

Highlights

- Rational design of indolenine dyes for *J*-aggregate formation
- Dyes exhibit unusually large Stokes shifts in both aggregates and crystals
- *J*-aggregates and protonation enable solid-state two-photon excited fluorescence
- Crystals exhibit reversible vapochromism for acid/base sensing

Authors

Carlos Benitez-Martin, Yolanda Vida, Duane Choquesillo-Lazarte, Enrique R. Losilla, Aurelio Cabeza, Francisco Najera, Ezequiel Perez-Inestrosa

Correspondence

carlos.benitez-martin@gu.se (C.B.-M.), najera@uma.es (F.N.), inestrosa@uma.es (E.P.-I.)

In brief

Benitez-Martin et al. report a rational design strategy to create small indolenine dyes that spontaneously form *J*-aggregates. The aggregates exhibit unusually large Stokes shifts and underpin the observation of solid-state two-photon excited fluorescence. Furthermore, the crystals display reversible vapochromic responses, proving suitable for developing robust and simple sensing devices.

Benitez-Martin et al., 2026, Cell Reports Physical Science 7, 103509
September 16, 2026
https://doi.org/10.1016/j.xcrp.2026.103509

CellPress

Cell Reports
Physical Science

CellPress
OPEN ACCESS

Article

J-aggregation in indolenine dyes drives fluorescent crystals with large Stokes shifts and two-photon excited emission

Carlos Benitez-Martin,[1,2,3,4,8,*] Yolanda Vida,[3,4,7] Duane Choquesillo-Lazarte,[5] Enrique R. Losilla,[6,7] Aurelio Cabeza,[6,7] Francisco Najera,[3,4,*] and Ezequiel Perez-Inestrosa[3,4,7,*]

[1]Department of Chemistry and Molecular Biology, University of Gothenburg, Medicinaregatan 19, 413 90 Göteborg, Sweden
[2]Department of Chemistry and Chemical Engineering, Chemistry and Biochemistry, Chalmers University of Technology, 412 96 Göteborg, Sweden
[3]Departamento de Química Orgánica, Universidad de Málaga, Andalucía-Tech Campus Teatinos S/n, 29071 Málaga, Spain
[4]Instituto de Investigación Biomédica de Málaga y Plataforma en Nanomedicina–IBIMA, Plataforma Bionand, Parque Tecnológico de Andalucía, 29590 Málaga, Spain
[5]Laboratorio de Estudios Cristalográficos, IACT-CSIC, Avda. de Las Palmeras 4, Armilla, 18100 Granada, Spain
[6]Departamento de Química Inorgánica, Facultad de Ciencias, Universidad de Málaga, Andalucía-Tech Campus Teatinos S/n, 29071 Málaga, Spain
[7]Instituto Universitario de Materiales y Nanotecnología, IMANA, University of Málaga, Campus de Teatinos, 29071 Málaga, Spain
[8]Lead contact
*Correspondence: carlos.benitez-martin@gu.se (C.B.-M.), najera@uma.es (F.N.), inestrosa@uma.es (E.P.-I.)
https://doi.org/10.1016/j.xcrp.2026.103509

SUMMARY

Organic fluorescent solids are highly demanded for applications such as sensing and bioimaging, yet most of these systems require co-crystallization with additional components to avoid aggregation-caused quenching. Here, the intermolecular assembly and resulting photophysical properties of a series of indolenine-based dyes are described. These dipolar donor-π-acceptor (D-π-A) structures are composed to favor head-to-tail interactions, rendering most of them with an exceptional ability for *J*-aggregate formation. Due to their tailored molecular architecture, *J*-aggregation features pair with unusually large Stokes shifts in both concentrated solutions and solid state (up to 3,272 cm^{-1} in aggregates and 6,135 cm^{-1} in solid state), enabling two-photon excited fluorescence (2PEF). Unlike most 2PEF-active condensed organic systems, these dyes spontaneously form single-component fluorescent crystals upon solvent evaporation, i.e., without requiring co-crystallization with additional components. The resulting crystals exhibit a pronounced and fully reversible vapochromic response, readily allowing the development of simple and robust sensing devices.

INTRODUCTION

With increasing relevance in materials science, organic luminescent dyes find extensive use in a plethora of applications. Particularly noteworthy are those exploiting two-photon excited fluorescence (2PEF), where the remarkable versatility of these materials meets the inherent advantages of multiphoton absorption processes. This synergy has made small-molecule-based materials seminal for the development of diverse technologies, including optical data storage,[1–4] upconverted lasing,[5–7] all-optical switching,[8–10] and bioimaging.[11–18]

Despite their technological potential, extending the use of organic fluorophores to the solid state remains challenging, and the majority of these applications are largely limited to the solution state: most organic fluorophores simply undergo aggregation-caused quenching (ACQ) upon assembly. Typically arising from strong π-π stacking interactions, ACQ leads to weak fluorescence in aggregated and/or solid states.[19–21] The opposite phenomenon, termed by Tang and co-workers in 2001 as aggregation-induced emission (AIE),[22] thus marked a turning point in the design of novel fluorophores for condensed-phase applications.[23] Among the various mechanisms proposed to explain AIE, as well as aggregation-induced emission enhancement (AIEE), the most commonly invoked mechanisms are (1) the restriction of intramolecular rotations in the aggregated state,[24,25] (2) the presence of a twisted intramolecular charge transfer (TICT),[26,27] and (3) *J*-aggregation.[28,29]

Focusing on *J*-aggregation, this phenomenon was reported for the first time by Jelley back in 1936.[30] The recent connection between *J*-aggregation and AIE has, however, sparked new interest in the ad hoc formation of such assemblies,[31–34] for which slipped-stack packing rather than co-facial packing is essential to guarantee *J*-type exciton coupling and preclude ACQ.[35,36] Essentially, this packing mode promotes both excitonic coupling and structural rigidification. On the one hand, the exciton coupling concentrates the oscillator strength into the lowest-energy exciton state, allowing radiative emission to outcompete non-radiative decay pathways. On the other hand, the tight intermolecular packing

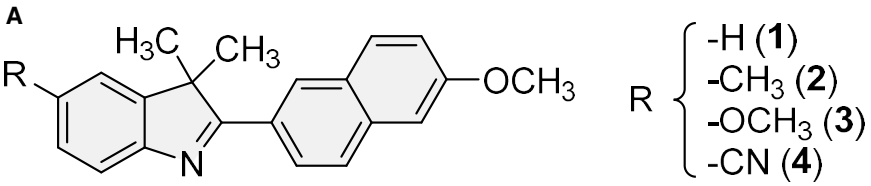

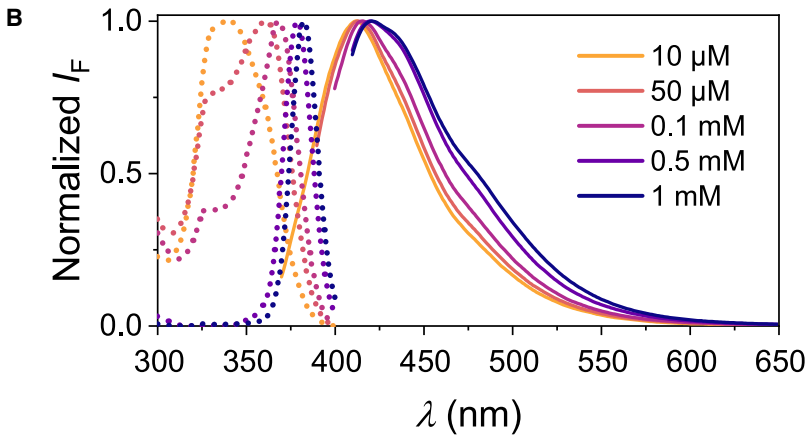

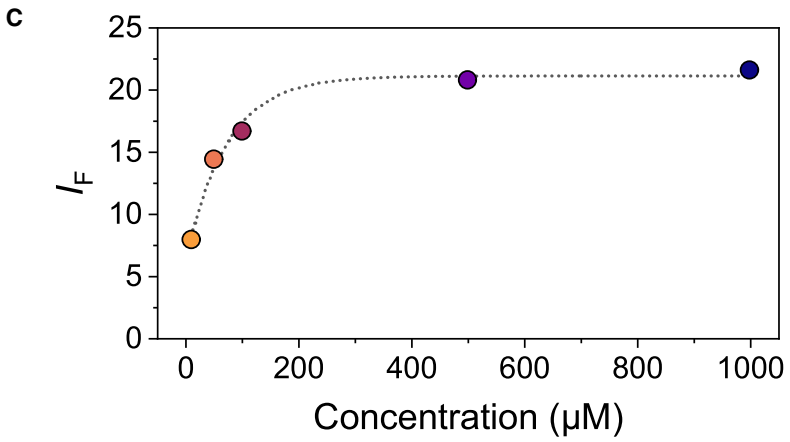

Figure 1. *J*-aggregate formation in acetonitrile

(A) Structures of derivatives **1**–**4**.

(B and C) For compound **1**, in acetonitrile, (B) normalized excitation (dashed lines) and emission (solid lines) spectra at different concentrations and (C) fluorescence intensity dependence on the concentration in acetonitrile.

restricts molecular motion, which further suppresses non-radiative mechanisms. Because of the fluorescence enhancement, the bathochromic shifts, and the exciton migration characterizing *J*-aggregates, diverse molecular architectures have been tailored to preferentially form such assemblies. Representative examples are cyanines,[37,38] squaraines,[39,40] chlorins,[41,42] perylene bisimides,[43,44] or BODIPYs.[45,46] The control of the intermolecular interactions at the supramolecular level, however, remains intricate: compounds displaying *J*-aggregation primarily stem from serendipity. As such, rational design strategies toward dyes with the ability to *J*-aggregate represent a valuable goal in organic materials science development.

Here, we develop a rational design strategy aimed at promoting *J*-type aggregation using a compact donor-π-acceptor (D-π-A) scaffold based on our previously reported 2-(6-methoxynaphthalen-2-yl)-3,3-dimethyl-*3H*-indole. Whereas the dipolar nature of this structure promotes head-to-tail interactions required for *J*-aggregation, the incorporation of the voluminous geminal methyl groups at position 3 efficiently disrupts π-π stacking and thus prevents ACQ effects. Various substituents are carefully introduced at position 5 to impart different photophysical properties as well as promote alternative crystalline packing orders without disrupting the head-to-tail alignment. Unlike conventional *J*-aggregate platforms, these molecules are characterized by a considerably smaller size, forming predominantly *J*-aggregates in solution and single-component crystals in the solid state. The unique features of these dyes yield *J*-aggregates with unusually large Stokes shifts (up to 3,272 cm^{-1}), which are the largest values reported for *J*-aggregates to the best of our knowledge. The marked bathochromic shifts in the excitation energies, on the other hand, make 2PEF exclusively for the highly ordered arrangements (aggregates or crystals) and facilitate two-photon absorption (2PA) in the solid state without the need for a co-crystallization process. This feature is highly desirable for the development of solid-state stimuli response fluorescence materials required for multitude of sensor-like applications. In light of our previous observations for this family of dyes[15] and considering the photophysical properties observed in condensed phase, we eventually investigate their response toward acid both in solution and in the solid state.

RESULTS AND DISCUSSION

Design and synthesis

Based on 2-(6-methoxynaphthalen-2-yl)-3,3-dimethyl-*3H*-indole (compound **1** in Figure 1A), three analogs, **2**–**4**, were prepared (Figure 1A). The detailed synthetic procedures and their structural characterization are described in supplemental methods and Figures S1–S15.

In the following, we describe the spectroscopic characterization of these compounds from highly diluted solution, through aggregate formation, to solid state. The structural studies and

Table 1. Photophysical properties of compounds 1–4 in different ordered states

	Solution								Solid state			
	Acetonitrile[a]				Aggregated[b]				Crystal			
	λ_{abs}[c]	λ_{em}[c]	$\Delta\nu$[d]	Φ_F[e]	λ_{abs}[c]	λ_{em}[c]	$\Delta\nu$[d]	Φ_F[e]	λ_{abs}[c]	λ_{em}[c]	$\Delta\nu$[d]	Φ_F[e]
1	339	413	5285	0.01[f]	384	421	2425	0.03[g]	391	421	3129	0.10[g]
2	344	418	4451	0.04[f]	387	424	2254	0.04[g]	370	423	3386	0.19[g]
3	351	416	5201	0.33[f]	391	435	2586	0.28[g]	370	431	3825	0.50[g]
4	352	440	5680	0.22[f]	393	451	3272	0.29[g]	372	482	6135	0.30[g]

[a]10 μM air-equilibrated solution.
[b]1 mM air-equilibrated solution.
[c]Absorption or emission wavelength, in nm.
[d]Stokes shift, in cm^{-1}.
[e]Fluorescence quantum yield, error ca. 15%.
[f]Measured according to the IUPAC standard-comparison method.[47]
[g]Measured with an integrating sphere.

theoretical calculations complete the properties picture of these compounds. Finally, we show how the overall photophysical features of these compounds can be readily harnessed into a simple sensing device.

Photophysical studies from solution to solid state

In solution

Highly diluted solutions. The photophysical properties of these derivatives were first studied in highly diluted solutions (10 μM) across a series of solvents of varying polarity (Table S1). Under these conditions, all compounds exhibit broad, structureless absorption and emission bands. Despite their dipolar character, solvatochromic effects are almost negligible, i.e., polarity-induced shifts in absorption and emission bands do not exceed 10 nm in any of the cases. Regarding the differences within the series, these are primarily governed by the substituent introduced at position 5, that is, by how this group modulates the electron-acceptor character of the *3H*-indole ring. Thus, compounds **1** (H) and **2** (CH_3) display similar features, whereas the inductive effects from methoxy and nitrile moieties in **3** and **4** are responsible for the relative observed bathochromic shifts. Higher fluorescence quantum yields are also observed for **3** and **4** (Table S1). Among their features, the most exceptional are the large Stokes shifts in the whole series (ca. 5,000 cm^{-1}; Table S1). The UV absorption of all compounds (bands centered between 330 and 360 nm) together with the weak influence of polarity practically precludes two-photon excitation (2PE) under highly diluted conditions.

Concentrated solutions and the formation of aggregates. Once the molecular behavior of our dyes was established under dilute conditions, we sought to delve into the aggregation phenomena. Self-assembly was induced by increasing the concentration of the compounds from 10 μM to 1 mM in acetonitrile, and the emission and excitation spectra were recorded (see Figure 1B for compound **1**; spectra for the other derivatives are in Figure S16). Given the high concentration required for the observation of *J*-aggregates, we opted for using excitation instead of absorption for these studies to avoid saturation issues (see Figure S30).

Gradual packing of these compounds produces bathochromic shifts considerably more pronounced in excitation (>40 nm) than in emission (<20 nm; see Table 1). Excitation bands also narrow with increasing concentration, which is further accompanied by fluorescence enhancement (Figure 1C). Notably, these features collectively represent clear hallmarks of *J*-aggregation and are observed within the whole series of dyes (Figure S16). The asymmetric displacements of excitation and emission energies with increasing concentration entails somewhat reduced Stokes shifts in the aggregated forms of our compounds when compared to highly diluted conditions. However, the Stokes shifts in the aggregated form of our dyes, over 2,200 cm^{-1} in all cases (Table 1), improve by far the previously reported values in literature for similar assemblies, typically falling in the range between 100 and 500 cm^{-1}. The large Stokes shifts of these aggregates are related to the intrinsic features of their monomers: although *J*-aggregation usually reduces the Stokes shifts, our constituent dyes feature large Stokes shifts when compared to other scaffolds that commonly form *J*-aggregates, such as those mentioned in the introduction.

Solid state

Single-component microcrystalline powders of all compounds formed spontaneously upon evaporation of dichloromethane solutions. Their optical properties were in turn investigated, and the main characterization data are summarized in Table 1.

Unlike the extremely narrow excitation bands of solution aggregates, the corresponding excitation bands of crystals display an important but expected broadening. It is worth noting that peak wavelengths and band spectral positions remain essentially unaltered among aggregates and crystals (Figure 2A for compound **1**; see Figure S17 for the other analogs), which points toward the highly ordered molecular packing from aggregates being preserved in the crystalline state. The importance of the evaporation rate was also examined, whereby we concluded that this solely affects the size of the crystals without disturbing their overall photophysics. Fluorescence quantum yields were determined and ranged from 0.10 in **1** to 0.50 in **3** (Table 1), further proving the occurrence of AIE (**1** and **2**) or AIEE (**3** and **4**) phenomena in the solid state depending on the compound considered. A more detailed explanation about the trends in fluorescence quantum yields according to electronic effects and crystal structure is provided below.

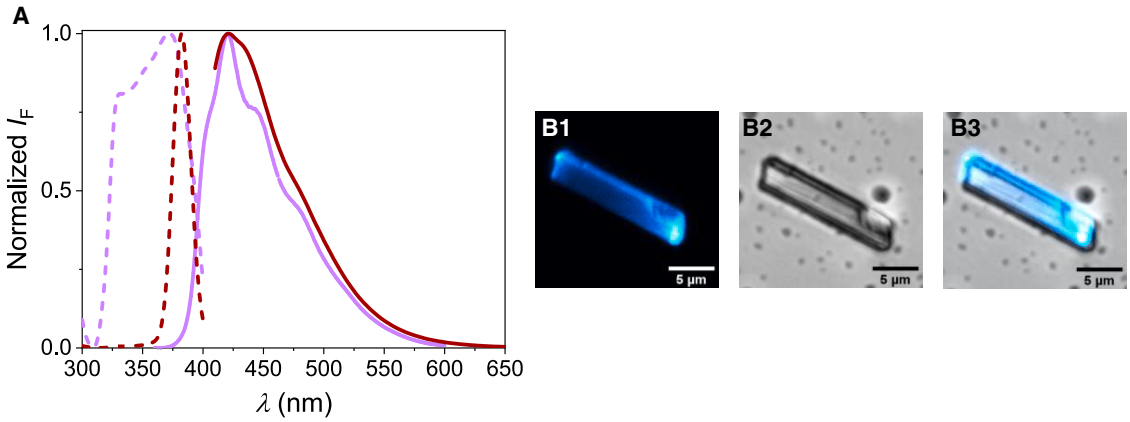

Figure 2. Solution aggregates vs. solid-state crystals

(A) Comparison for compound **1** between the emission (solid lines) and excitation (dashed lines) spectra of the aggregates in 1 mM acetonitrile solution (dark-red lines) and the crystals (violet lines).

(B) b1: fluorescent imaging of a microcrystal upon 2P excitation at 700 nm. b2: white-field imaging of the previous microcrystal. b3: superposition of b1 and b2 images. Scale bars, 5 μm.

Under two-photon conditions

The observed bathochromic shifts in the excitation energies of the packed forms enabled their characterization under two-photon (2P) conditions, and 2PE and 2PEF were recorded for both aggregates and crystals (Figures S18–S21). It is worth noting that this 2PA response, not observable under diluted conditions, is a collective photophysical consequence of the intramolecular charge-transfer character of the chromophores further potentiated by the exciton coupling inherently associated with the formation of *J*-aggregates.

The 2PEF imaging of crystals, shown in Figure 2B for a microcrystal of compound **1**, newly revealed that there are no differences in the optical properties related to the size of the crystal, as evident when comparing them with those determined from the microcrystalline powder. Importantly, the 2PEF spectra resembled those obtained under one-photon (1P) excitation conditions for all compounds (Figure S18 for aggregates and Figure S20 for crystals), thus confirming that identical emissive states are reached regardless of the nature of the excitation process. It is very important to emphasize that 2PE and 2PEF, for all dyes, were uniform across the laser focal area, yielding only variations in the intensity observed (see normalized spectra in Figure S20). Eventually, the square dependence of the emission on the excitation power verified the biphotonic nature of both aggregates (Figure S19) and crystals (Figure S20).

Unveiling *J*-aggregation from the structure

Crystal structure studies

To elucidate the intermolecular interactions governing the solid-state assembly and driving the *J*-aggregation phenomena, the crystalline structures of compounds **1**–**4** were determined via X-ray diffraction (XRD). Details about the different crystalline structures observed for these dyes are duly presented in the supplemental information. Transmission electron microscopy (TEM) further confirmed the formation of uniform microcrystalline domains (Figure 3A).

The analysis of the crystalline structures reveals three key features underpinning *J*-aggregate characteristics.

(1) Head-to-tail packing and space group symmetry. While the compounds crystallize in different ways, a dominant head-to-tail packing is preserved across all structures along the crystallographic axes (Figures 3B and 3C). This alignment enables dipole-dipole interactions that facilitate *J*-type exciton coupling and consequent fluorescence emission enhancement. In detail, compound **1** crystallizes in an orthorhombic $Pna2_1$ space group, where the crystal packing is governed by weak non-classical intermolecular interactions including mainly aromatic $CH\cdots OCH_3$ and $OCH_3\cdots OCH_3$ interactions. The incorporation of a methyl group in **2** is responsible for this dye adopting a centrosymmetric monoclinic $P2_1/c$ space group, where the increased molecular volume increases the close-packing efficiency within the crystal lattice and the head-to-tail alignment is sustained primarily by $CH_3\cdots OCH_3$ interactions among the methyl groups and oxygen atoms of neighboring molecules. Compound **3**, however, crystallizes in the lower-symmetry $P2_1$ monoclinic group, and its packing is dominated by highly directional and strong intermolecular $OCH_3\cdots OCH_3$ hydrogen bonds linking neighboring molecules along the 2_1 axes. In relation to compound **4**, this adopts the $P2_1/c$ space group, displaying a structure strongly influenced by the electronic effects of the nitrile group. In particular, the crystal framework is predominantly governed by antiparallel dipolar arrangements, with the head-to-tail alignment specifically dictated by $OCH_3\cdots NC$ hydrogen bonds.

(2) Suppression of π-π stacking. Seminal for the formation of *J*-aggregates is the suppression of these interactions and related ACQ effects, which requires an interaromatic centroid distance (in our case, determined as the distance between a certain indolenine ring and the nearest

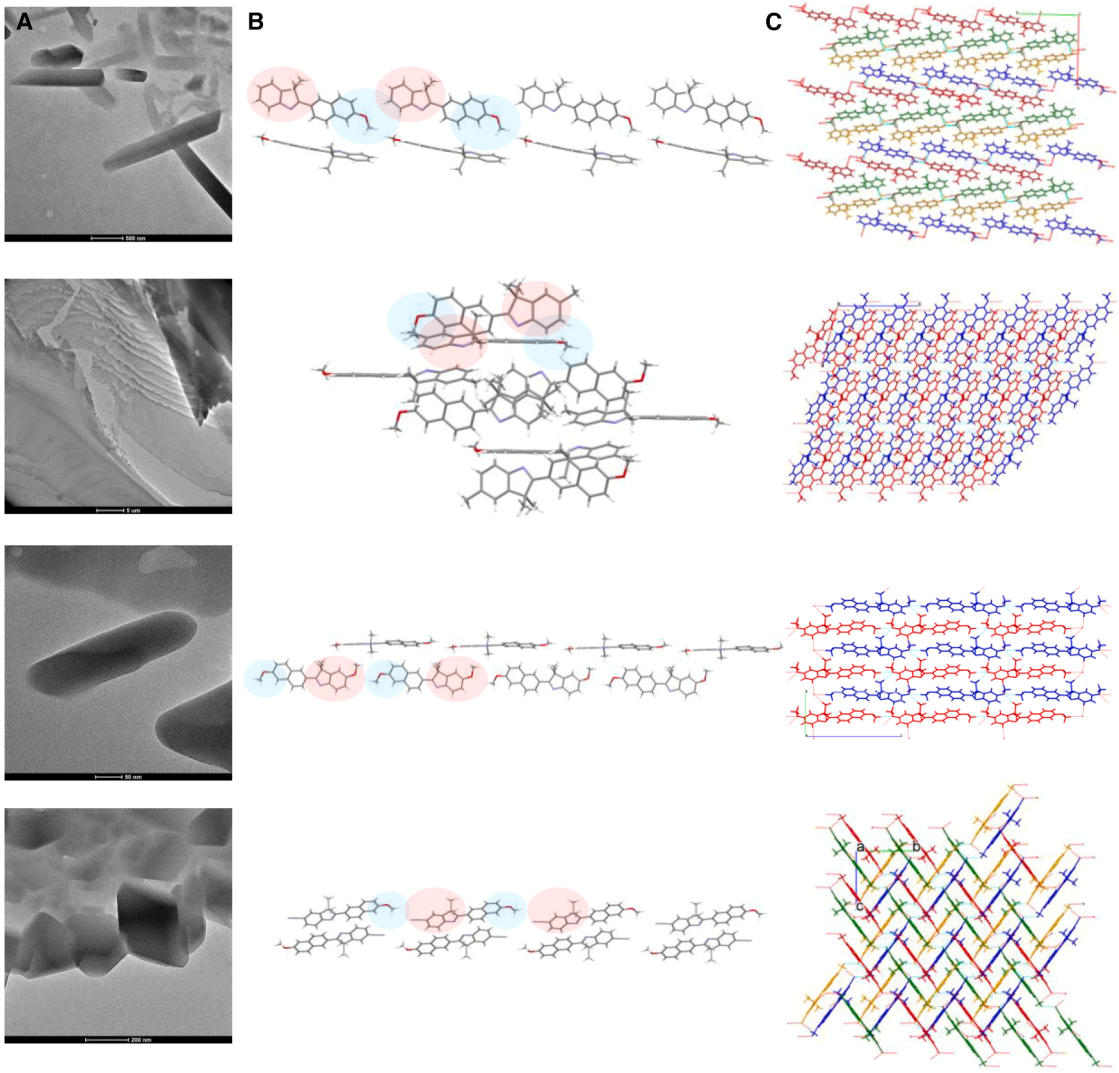

Figure 3. Crystals of compounds 1–4

(A) TEM images of the crystals of compounds **1**–**4** (top to bottom). Scale bars (top to bottom), 500 nm, 5 μm, 50 nm, and 200 nm.

(B) Head-to-tail alignment of compounds **1**–**4** in their crystals (top to bottom); donor and acceptor groups are highlighted in blue and red, respectively, for better visualization.

(C) Different views of the crystal structure of compounds **1**–**4** (top to bottom). The head-to-tail alignments across the crystals are represented in this case by different colors.

aromatic center, either naphthalene or another indolenine unit) of at least 4.0 Å. Compounds **1**, **2**, and **3** fulfill this requirement, with minimum observed interaromatic centroid distances of 6.08, 6.16, and 6.76 Å, respectively. Compound **1** is further characterized by stabilizing its architecture through multiple edge-to-face CH · · · Ar interactions between aromatic hydrogen atoms and adjacent aromatic ring centroids. In compound **3**, weak methoxyarene (OCH_3 · · · Ar) interactions are present, facilitating the interdigitation of hydrophobic aromatic domains between adjacent molecular layers. In the case of derivative **4**, the interaromatic-centroid distance is slightly shorter (3.81 Å), posing a slightly different situation in comparison to the other analogs. This compressed distance allows for the formation of centrosymmetric inversion dimers through complementary π-π stacking interactions between neighboring planar aromatic cores, contributing to lattice stabilization and allowing the simultaneous formation of both *J*- and *H*-aggregates. Nevertheless, the overall optical properties point toward intermolecular interactions of predominantly dipole-dipole nature (Figure S22). Although near-planar conformations are observed, featuring an indolenine-naphthalene dihedral angle that ranges from 8° to 23° (Table S3), the scaffolds are sterically shielded by the geminal dimethyl groups at position 3 that efficiently impede π-π interactions.

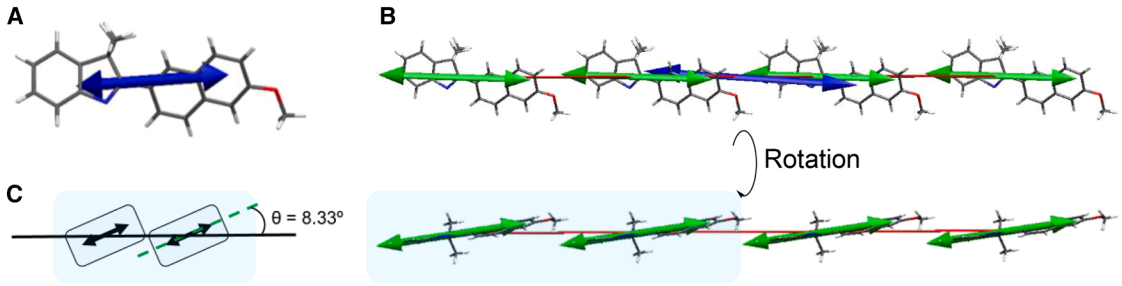

Figure 4. TDDFT analysis of the aggregate excitons

(A) Transition dipole moment (TDM), represented in blue, for the $S_0 \rightarrow S_1$ transition of compound **1**.

(B) Different views of the crystal structure of compound **1**. Individual TDMs are indicated in green, while the TDM of the tetramer is represented in blue.

(C) Schematic representation of the TDMs and the slip angle with respect to the line crossing centers of mass of the molecules composing the tetramer.

(3) Hydrogen-bond reinforcement. These interactions further strengthen the assembling in the crystalline structure, facilitating efficient dipole-dipole interactions as mentioned before: $OCH_3 \cdots O$ for compounds **1** and **3**, $OCH_3 \cdots NC$ for **4**, and $Ar\text{-}CH_3 \cdots OCH_3$ for **2** (Tables S4–S7 and supplemental methods).

All in all, these four compounds achieve *J*-aggregate-favoring crystal-packing motifs through complementary supramolecular pathways. Compounds **1** and **2** rely predominantly on weak $CH \cdots OCH_3$ interactions, and the higher steric hindrance in **2** accounts for its improved fluorescence quantum yield in solid state. Compounds **3** and **4** display a more highly directional assembly driven by methoxy- and nitrile-mediated heteroatom interactions, where the charge transfer character plays an important role (see Table S11). In this case, to explain the differences in fluorescence quantum yields, electronic effects must be also considered: the incorporation of a methoxy group increases the electron-acceptor character of the indolenine ring, favoring the formation of intramolecular charge transfer (ICT) states from which the fluorescence stems. Replacing this substituent by nitrile in **4** should promote even further the efficiency of the ICT and result in a higher fluorescence quantum yield, but the shorter interaromatic distances counterbalance this effect by allowing π-π stacking interactions, thus affecting negatively the fluorescence emission efficiency and explaining the observed trends.

Theoretical calculations

Time-dependent density functional response theory (TDDFT) calculations were performed to gain additional insights into how the optical properties of these compounds are dependent on the structural configuration and the packed arrangements. In particular, the lowest energy electronic transitions from the ground electronic state were calculated in both the isolated solvated molecules (Table S8 and Figure S23) and their respective aggregates (Table S9). For the aggregates, "tetramers" were selected from the crystal structure, and no further geometry optimization was performed.

In the absence of intermolecular interactions, the highest occupied molecular orbital-lowest unoccupied molecular orbital (HOMO-LUMO) energy gaps of the isolated molecules are dictated by the electron-donor or electron-acceptor character of the substituent at position 5 (Table S8). As previously mentioned, these substituents operate via inductive effects, modulating the overall electron-acceptor character of the indolenine ring accordingly.

Interestingly, the trends found in the aggregates follow a pattern similar to those identified in the isolated molecules, i.e., their electronic properties are driven overall by the decoration on the indolenine ring. Thereby, the introduction of substituents at position 5 mainly contributes to destabilizing the respective occupied frontier orbitals, resulting in decreased HOMO-LUMO energy gaps across the series (Table S9). This behavior would account for the bathochromic shifts observed upon aggregation for each compound. On the other hand, the individual transition dipole moments (TMDs) seem to be oriented along the long axis of the molecule (Figure 4A), and, moreover, these are aligned with the line crossing the centers of mass of the molecules composing the tetramer. The small angle between the individual TMDs (θ) translates into efficient exciton coupling, a hallmark of *J*-aggregation, which is manifested by a substantially larger TMD for the aggregate (Figures 4B, 4C, and S24).

Application as sensors for acid environments

Bearing in mind the previously reported ability of related structures as proton sensors,[15] we finally decided to exploit this feature of the dyes. Thus, their optical properties were evaluated in the presence of acid both in solution and in solid state.

Highly diluted solutions

For measurements in highly diluted (10 μM) aqueous environments, acidic conditions were established by using hydrochloric acid buffer at pH 1.2. Under these conditions, and as to some extent envisaged, both absorption and emission bands are drastically shifted to longer wavelengths for all compounds. This is a consequence of the increase in the electron-acceptor character of the indolenine ring upon protonation, which enhances the electronic delocalization within the push-pull system and reduces the HOMO-LUMO gap. More specifically, the absorption of **1H**–**4H**, the protonated versions of **1**-**4**, display bands centered around 400 nm paired with emission peaks in the blue-to-green spectral region between 500 and 540 nm (Table 2 and Figure S25). It is worth noting not only that all these trends were reproduced satisfactorily by TDDFT (Figure S26 and

Table 2. Photophysical properties of compounds 1–4 in neutral and acidic conditions

	Conditions	λ_{abs}[a]	λ_{em}[a]	$\Delta\nu$[b]	Φ_F[c]	σ_{2PA} (GM)[d]
1	H_2O[e]	337	438	6,843	0.14	–[f]
1-H	HCl_{aq}[e]	400	502	5,080	0.37[g]	59 (800)
	crystal + HCl_g	–[f]	544	11,921	0.07[h]	–[f]
2	H_2O[e]	344	439	6,291	0.17	–[f]
2-H	HCl_{aq}	404	502	4,832	0.37[g]	32 (800)
	crystal + HCl_g	–[f]	541	11,727	0.05[h]	–[f]
3	H_2O[e]	351	448	6,169	0.49	–[f]
3-H	HCl_{aq}	412	526	5,260	0.06[g]	19 (830)
	crystal + HCl_g	–[f]	557	9,295	0.07[h]	–[f]
4	H_2O[e]	352	478	7,489	0.60	–[f]
4-H	HCl_{aq}	412	511	4,702	0.10[g]	36 (830)
	crystal + HCl_g	–[f]	516	7,647	0.21[h]	–[f]

[a]Wavelength, in nm.
[b]Stokes shift, in cm^{-1}.
[c]Fluorescence quantum yield, error ca. 15%.
[d]2PA cross-sections were measured in the range of 700–1,000 nm in 10 μM solutions; the corresponding 2PA wavelength (nm) is provided in parentheses.
[e]10 μM air-equilibrated solution.
[f]Not measured.
[g]Measured according to the IUPAC standard-comparison method.
[h]Measured with an integrating sphere.

Table S10), but also that the emission spectra are not dependent on the nature of the excitation source.

The shifts in the absorption energies upon protonation are particularly interesting, as they allow biphotonic excitation of the protonated species under diluted conditions. The activation of the 2PA properties by protonation is associated with the increase of the ICT character of the dyes, implying a bathochromic shift in the excitation energies different from that attained by the formation of aggregates and thus constituting an alternative way in addition to *J*-aggregation to obtain a 2PA response. Thus, the 2PA properties of the **1H–4H** were investigated via a 2P-induced fluorescence method.[48] These compounds show moderate 2PA cross-section values (σ_{2PA}) from 19 to 59 Goeppert-Mayer units (GM) (Table 2 and Figure 5). Furthermore, reversibility studies were performed by sequential exposure of the solutions to hydrochloric acid and/or ammonia vapors in 30-s periods, whereby the spectral properties of all compounds were maintained after several interconversion cycles (Figure S27).

Solid state

The optical properties of microcrystals of compounds **1–4** were studied after these were exposed to hydrochloric acid vapors. As anticipated, important bathochromic shifts were observed in their emission (Tables 1 and 2) independently of the nature of the excitation source (one or two photons). More concretely, protonation of all crystals comes with an almost 100-nm shift in the fluorescence peak, which is especially pronounced for **3** (Figure S28). Interestingly, XRD measurements carried out on a single crystal point to protonation as a surface phenomenon, as no changes were observed in the crystalline structures with respect to those of the neutral forms. Thus, the observed

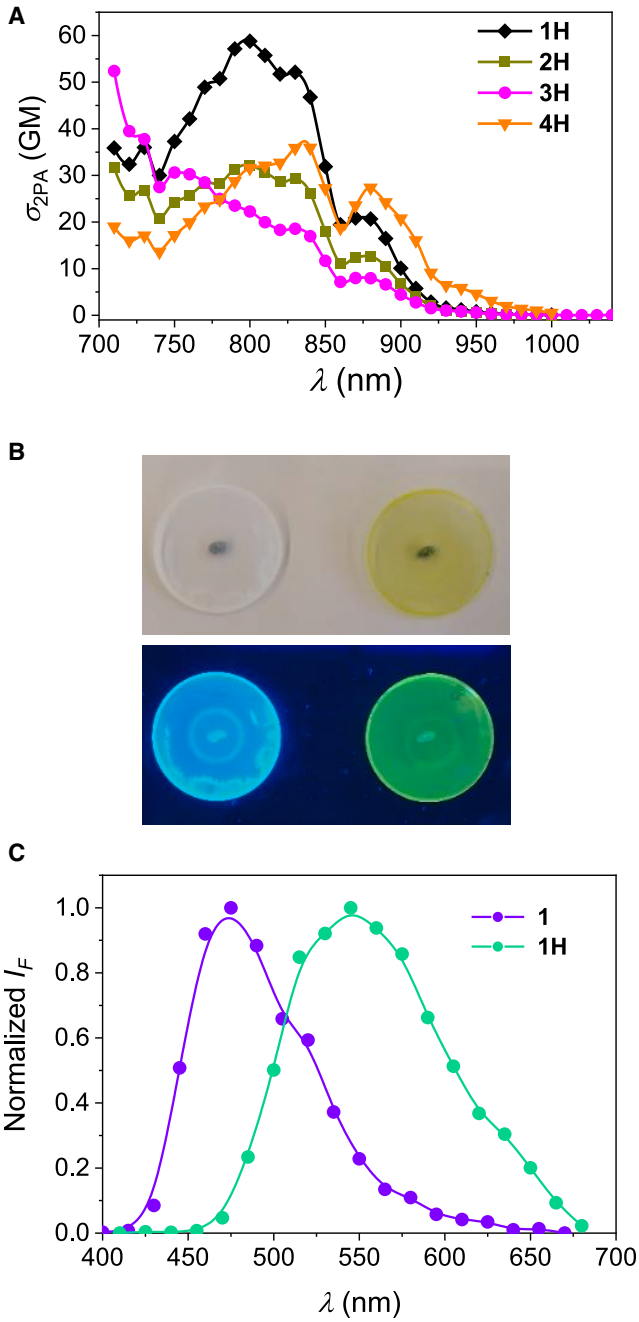

Figure 5. Reversible acid-vapor sensing

(A) 2PA cross sections for compounds **1–4** in hydrochloric acid aqueous solutions (pH 1.2) at 10 μM.

(B) Devices to sense acid vapors. These were made by depositing **1** in a glass surface (0.17 mm thickness) by spin-coating deposition method. The device at the left is shown in the neutral state, while the one on the right has been exposed to hydrochloric acid vapors for 30 s. The top row shows the aspect seen with naked eye, while the bottom corresponds to 365-nm illumination from a handheld lamp.

(C) Two-photon excited fluorescence spectra for compound **1** (spin coating, λ_{exc} = 720 nm) under neutral (purple) and acid (green) conditions.

bathochromic shifts are mostly related to the protonation-enhanced ICT character of the dyes, although contributions from pre-existing solid-state packing cannot be discarded.

Due to the potential application of new-generation stimuli-response fluorescence systems for diverse applications, a direct use of compound **1** as an acid/base sensor was tested. This dye was deposited over a glass surface (0.17 mm thickness) using a spin-coating deposition method, whereby photophysics comparable to those observed in solid state for compound **1** were determined. The exposure to vapor acids yields changes that are not only monitored through fluorescence readout but also can be appreciable via the naked eye, under either 1P or 2P excitation (Figures 5B and 5C). Similarly to solution, reversibility studies were performed by sequential exposure of the spin-coating device to hydrochloric acid and ammonia vapors in periods of 30 s, whereby the spectral properties of derivative **1** were maintained after several interconversion cycles (Figure S29).

The findings presented here validate our rational D-π-A design strategy, uncovering small indolenine dyes as a potential *J*-aggregate platform in solution and solid states, further characterized by unusually large Stokes shifts. These compounds additionally showed ability to spontaneously form single-component crystals exhibiting solid-state 2PEF and reversible vapochromism. Although this dye platform overcomes key limitations of conventional *J*-aggregates, mainly related to the extensive spectral overlap between absorption and emission, important challenges yet remain to be circumvented, such as, for instance, extending the absorption into longer wavelengths for potential application in bioimaging and/or tuning emission color across the series for the development of more sophisticated detection devices. Success in these new avenues could potentially establish these compact dyes as versatile building blocks for nonlinear optics, lasing, multiplexed sensing arrays, and stimuli-responsive materials, ultimately driving *J*-aggregation from serendipitous discovery to engineered functionality.

METHODS

General methods and instrumentation

Unless otherwise stated, commercially available reagents and solvents were purchased and used as supplied. Column chromatography was performed using silica gel 60 (230–400 mesh) and thin-layer chromatography with silica gel 60 F_{254} plates. The precursors for compounds **1**–**4** and compound **1** were synthesized according to our previously reported procedures.[16] All the synthesized chemical structures were corroborated from their NMR spectra (either monodimensional and bidimensional), their mass spectrometry data, and their infrared data. NMR spectra were collected on a Bruker Avance III Ascend 400-MHz spectrometer at 25°C. ^{1}H NMR and ^{13}C NMR chemical shifts (δ) are indicated in parts per million (ppm). These were referenced to the residual solvent peak specific of DMSO-d_6 (CHD_5SO at 2.50 ppm and $(CD_3)_2SO$ at 39.5 ppm for ^{1}H NMR and ^{13}C NMR, respectively). Total assignment of the NMR shifts was carried out with 2D NMR experiments (correlation spectroscopy [COSY], heteronuclear single-quantum coherence [HSQC], and heteronuclear multiple-bond correlation [HMBC]) as appropriate. High-resolution electrospray ionization mass spectra were obtained on a Thermo Fisher high-resolution mass spectrometer (Orbitrap), and infrared spectra were recorded on a JASCO FT/IR-4100. Melting points were measured in a Gallenkamp melting-point apparatus. TEM images were obtained with a Thermo Scientific FEI Tecnai G2 20 twin-transmission electron microscope.

One-photon photophysical properties

Spectroscopic-grade solvents were employed for all the photophysical studies. Experiments were performed at room temperature with either optically diluted or 10 μM air-equilibrated solutions using 1-cm-pathlength quartz cuvettes. Absorption spectra were recorded on a Cary 100 Bio UV-visible spectrophotometer, and emission spectra were registered on a JASCO FP-750 instrument. Fluorescence quantum yields (ϕ_f) were determined by comparison with coumarin 153 (ϕ_f = 0.38 in ethanol) according to a literature procedure.[47]

Two-photon absorption properties

Two-photon-induced fluorescence emission for aggregates (spectroscopic-grade acetonitrile was employed to dissolve dyes **1**–**4** to a final concentration of 1 mM) and crystals were analyzed using an inverted Leica SP5 MP confocal and multiphoton microscope hosted at the ICTS NANBIOSIS, specifically in the U28 Unit of the Andalusian Center for Nanomedicine and Biotechnology (BIONAND). This microscope was equipped with a MaiTai Ti:Sapphire HP laser (Spectra-Physics) tunable between 690 and 1,040 nm. Imaging was performed using a 10× plan apochromatic objective lens (NA 0.4) focused at the air/liquid boundary, allowing for simultaneous detection of sample and background fluorescence. Emission and excitation spectra data for compound and background regions of interest were registered using Leica LAS AF software. Spectra were measured in a laser power regime where the fluorescence was proportional to the square of the laser excitation power and using a dynamic 15-nm-wide emission detection window moving in 20 steps from 400 to 700 nm.

Two-photon absorption (2PA) cross-sections (σ_{2PA}) were determined using the 2P-induced fluorescence method for compounds **1H**–**4H**.[48,49] Rhodamine B (10^{-7} M in air-equilibrated spectroscopic-grade methanol) was employed as the reference under experimentally identical conditions, considering the fluorescence quantum yield independent of the excitation regime. Hydrochloric aqueous solutions (pH 1.2) were employed to dissolve dyes **1H**–**4H** to a final concentration of 10 μM. All σ_{2PA} measurements were determined on two separate independent occasions and are presented as the mean value, with each pair of replicates differing by no more than 10%.

XRD determination

Measured crystals were prepared under inert conditions immersed in perfluoropolyether as protecting oil for manipulation. Suitable crystals were mounted on MiTeGen micromounts, and these samples were used for data collection. Data were collected with a Bruker D8 Venture diffractometer with CuKα radiation (λ = 1.54178 Å). The data were processed with the APEX3 suite.[50] The structures were solved by intrinsic phasing using the ShelXT program, which revealed the position of all non-hydrogen

atoms. These atoms were refined on F^2 by a full-matrix least-squares procedure using the anisotropic displacement parameter.[51] All hydrogen atoms were located in difference Fourier maps and included as fixed contributions riding on attached atoms with isotropic thermal displacement parameters 1.2 or 1.5 times those of the respective atom. Olex2 software was used as a graphical interface.[52] The crystallographic data for the reported structures were deposited with the Cambridge Crystallographic Data Center as supplementary publication no. CCDC 2047498-2047501. Additional crystal data are shown in Table S2. Copies of the data can be obtained free of charge at http://www.ccdc.cam.ac.uk/products/csd/request.

Theoretical calculations

Isolated molecules

Theoretical calculations were performed with the Gaussian 16 program package.[53] The polarizable continuum model[54] was used to consider the solvent effect and acetonitrile or water as solvent. The starting geometries for compounds **1–4** were obtained from X-ray crystal data. The ground-state (S_0) and excited-state (S_1) geometrical parameters were determined by density functional theory (DFT) using the CAM-B3LYP[55] functional and the 6-31+G(d) basis set. In each optimization, the vibrational frequencies were calculated, whereby the absence of imaginary frequencies showed that optimized structures were true minima. Energy parameters were calculated as vertical electronic excitations using the linear response approach and TDDFT.

Tetramers

The geometries for the tetramers of compounds **1–4** were obtained from X-ray crystal data. Single-point and TDDFT calculations were performed using DFT and the CAM-B3LYP functional in the gas phase and the 6-31G(d) basis set. The charge transfer indices for the excited state S_1 were obtained with the Hole-Electron analysis module in the Multifunctional Wavefunction Analyzer (MULTIWFN v.3.8).[56,57]

RESOURCE AVAILABILITY

Lead contact

Further information and requests for resources should be directed to and will be fulfilled by the lead contact, Carlos Benitez-Martin (carlos.benitez-martin@gu.se).

Materials availability

This study did not generate new unique reagents.

Data and code availability

- Any additional experimental data required to reanalyze the results presented in this article will be shared upon reasonable request by the lead contact, provided it is not already included in the article or supplemental information.
- CCDC 2047498–20474501 contains supplementary crystallographic data for compounds **1–4**.
- This paper does not report original code.

ACKNOWLEDGMENTS

This work was supported by the Spanish Ministerio de Ciencia, Innovación y Universidades (grant PID2022-136705NB-I00), Junta de Andalucía (FQM-017), and FEDER Funds FPU fellowship (FPU16/02516) for C.B.-M. We gratefully acknowledge the computer resources provided by the SCBI (Supercomputing and Bioinformatics Center) of the University of Malaga.

AUTHOR CONTRIBUTIONS

C.B.-M., conceptualization, data curation, formal analysis, investigation, methodology, project administration, supervision, validation, visualization, writing – original draft, and writing – review & editing; Y.V., data curation, formal analysis, and writing – review & editing; D.C.-L., data curation, formal analysis, investigation, and resources; E.R.L., formal analysis and resources; A.C., formal analysis and resources; F.N., conceptualization, data curation, formal analysis, funding acquisition, investigation, project administration, supervision, validation, visualization, and writing – review & editing; E.P.I., funding acquisition, project administration, and supervision.

DECLARATION OF INTERESTS

The authors declare no competing interests.

SUPPLEMENTAL INFORMATION

Supplemental information can be found online at https://doi.org/10.1016/j.xcrp.2026.103509.

Received: February 23, 2026
Revised: June 4, 2026
Accepted: August 3, 2026

REFERENCES

1. Dvornikov, A.S., Walker, E.P., and Rentzepis, P.M. (2009). Two-photon three-dimensional optical storage memory. J. Phys. Chem. A *113*, 13633–13644. https://doi.org/10.1021/jp905655z.
2. Tian, H., and Feng, Y. (2008). Next step of photochromic switches? J. Mater. Chem. *18*, 1617–1622. https://doi.org/10.1039/b713216f.
3. Belfield, K.D., and Schafer, K.J. (2002). A new photosensitive polymeric material for WORM optical data storage using multichannel two-photon fluorescence readout. Chem. Mater. *14*, 3656–3662. https://doi.org/10.1021/cm010799t.
4. Zhou, H., Zhou, F., Tang, S., Wu, P., Chen, Y., Tu, Y., Wu, J., and Tian, Y. (2012). Two-photon absorption dyes with thiophene as π electron bridge: Synthesis, photophysical properties and optical data storage. Dyes Pigments *92*, 633–641. https://doi.org/10.1016/j.dyepig.2011.06.028.
5. Gao, F., Liao, Q., Xu, Z.Z., Yue, Y.H., Wang, Q., Zhang, H.L., and Fu, H.B. (2010). Strong Two-Photon Excited Fluorescence and Stimulated Emission from an Organic Single Crystal of an Oligo(Phenylene Vinylene). Angew. Chem. Int. Ed. *49*, 6243. https://doi.org/10.1002/anie.201090113.
6. Zhang, C., Zou, C.L., Yan, Y., Hao, R., Sun, F.W., Han, Z.F., Zhao, Y.S., and Yao, J. (2011). Two-Photon Pumped Lasing in Single-Crystal Organic Nanowire Exciton Polariton Resonators. J. Am. Chem. Soc. *133*, 7276–7279. https://doi.org/10.1021/ja200549v.
7. Guzelturk, B., Kanibolotsky, A.L., Orofino-Pena, C., Laurand, N., Dawson, M.D., Skabara, P.J., and Demir, H.V. (2015). Ultralow-threshold up-converted lasing in oligofluorenes with tailored strong nonlinear absorption. J. Mater. Chem. C Mater. *3*, 12018–12025. https://doi.org/10.1039/c5tc02247a.
8. Piccione, B., Cho, C.H., van Vugt, L.K., and Agarwal, R. (2012). All-optical active switching in individual semiconductor nanowires. Nat. Nanotechnol. *7*, 640–645. https://doi.org/10.1038/nnano.2012.144.
9. Gieseking, R.L., Mukhopadhyay, S., Shiring, S.B., Risko, C., and Brédas, J.L. (2014). Impact of Bulk Aggregation on the Electronic Structure of Streptocyanines: Implications for the Solid-State Nonlinear Optical Properties and All-Optical Switching Applications. J. Phys. Chem. C *118*, 23575–23585. https://doi.org/10.1021/jp507920j.

10. Benitez-Martin, C., Li, S., Dominguez-Alfaro, A., Najera, F., Pérez-Inestrosa, E., Pischel, U., and Andréasson, J. (2020). Toward Two-Photon Absorbing Dyes with Unusually Potentiated Nonlinear Fluorescence Response. J. Am. Chem. Soc. *142*, 14854–14858. https://doi.org/10.1021/jacs.0c07377.

11. Albota, M., Beljonne, D., Brédas, J.L., Ehrlich, J.E., Fu, J.Y., Heikal, A.A., Hess, S.E., Kogej, T., Levin, M.D., Marder, S.R., et al. (1998). Design of organic molecules with large two-photon absorption cross sections. Science *281*, 1653–1656. https://doi.org/10.1126/science.281.5383.1653.

12. Helmchen, F., and Denk, W. (2006). Deep tissue two-photon microscopy. Nat. Methods *3*, 235. https://doi.org/10.1038/nmeth0306-235.

13. Kim, H.M., and Cho, B.R. (2009). Two-Photon Probes for Intracellular Free Metal Ions, Acidic Vesicles, and Lipid Rafts in Live Tissues. Acc. Chem. Res. *42*, 863–872. https://doi.org/10.1021/ar800185u.

14. Yu, J., Cui, Y., Xu, H., Yang, Y., Wang, Z., Chen, B., and Qian, G. (2013). Confinement of pyridinium hemicyanine dye within an anionic metal-organic framework for two-photon-pumped lasing. Nat. Commun. *4*, 2719. https://doi.org/10.1038/ncomms3719.

15. Benitez-Martin, C., Guadix, J.A., Pearson, J.R., Najera, F., Perez-Pomares, J.M., and Perez-Inestrosa, E. (2020). Indolenine-Based Derivatives as Customizable Two-Photon Fluorescent Probes for pH Bioimaging in Living Cells. ACS Sens. *5*, 1068–1074. https://doi.org/10.1021/acssensors.9b02590.

16. Benitez-Martin, C., Guadix, J.A., Pearson, J.R., Najera, F., Perez-Pomares, J.M., and Perez-Inestrosa, E. (2019). A turn-on two-photon fluorescent probe for detecting lysosomal hydroxyl radicals in living cells. Sensor. Actuator. B Chem. *284*, 744–750. https://doi.org/10.1016/j.snb.2018.12.163.

17. Benitez-Martin, C., Marin-Beloqui, J.M., Navarrete, J.T.L., Casado, J., Najera, F., and Perez-Inestrosa, E. (2025). Counterintuitive Fluorescence Blue Shift in Symmetry Breaking Dicationic Bis(indolium) with Two-Photon Absorption Properties for NIR Living Cell Imaging. Adv. Mater. e10730. https://doi.org/10.1002/adma.202510730.

18. Benitez-Martin, C., Najera, F., and Perez-Inestrosa, E. (2025). Simultaneous dual-colour labelling of mitochondria and lysosomes: An indolium-based approach. Sensor. Actuator. B Chem. *423*, 136862. https://doi.org/10.1016/j.snb.2024.136862.

19. Chandross, E.A., and Dempster, C.J. (1970). Intramolecular Excimer Formation and Fluorescence Quenching in Dinaphthylalkanes. J. Am. Chem. Soc. *92*, 3586–3593. https://doi.org/10.1021/ja00715a010.

20. Jenekhe, S.A., and Osaheni, J.A. (1994). Excimers and Exciplexes of Conjugated Polymers. Science *265*, 765–768. https://doi.org/10.1126/science.265.5173.765.

21. Mei, J., Leung, N.L.C., Kwok, R.T.K., Lam, J.W.Y., and Tang, B.Z. (2015). Aggregation-Induced Emission: Together We Shine, United We Soar. Chem. Rev. *115*, 11718–11940. https://doi.org/10.1021/acs.chemrev.5b00263.

22. Luo, J., Xie, Z., Lam, J.W.Y., Cheng, L., Tang, B.Z., Chen, H., Qiu, C., Kwok, H.S., Zhan, X., Liu, Y., and Zhu, D. (2001). Aggregation-induced emission of 1-methyl-1,2,3,4,5-pentaphenylsilole. Chem. Commun. *37*, 1740–1741. https://doi.org/10.1039/b105159h.

23. Wang, B., Liu, Y., Chen, X., Liu, X.T., Liu, Z., and Lu, C. (2024). Aggregation-induced emission-active supramolecular polymers: from controlled preparation to applications. Chem. Soc. Rev. *53*, 10189–10215. https://doi.org/10.1039/d3cs00017f.

24. Petersen, A.U., Broman, S.L., Olsen, S.T., Hansen, A.S., Du, L., Kadziola, A., Hansen, T., Kjaergaard, H.G., Mikkelsen, K.V., and Nielsen, M.B. (2015). Controlling Two-Step Multimode Switching of Dihydroazulene Photoswitches. Chemistry (Easton). *21*, 3968–3977. https://doi.org/10.1002/chem.201405457.

25. Parrott, E.P.J., Tan, N.Y., Hu, R., Zeitler, J.A., Tang, B.Z., and Pickwell-MacPherson, E. (2014). Direct evidence to support the restriction of intramolecular rotation hypothesis for the mechanism of aggregation-induced emission: temperature resolved terahertz spectra of tetraphenylethene. Mater. Horiz. *1*, 251–258. https://doi.org/10.1039/c3mh00078h.

26. Göbel, D., Helbig, A., Friedrich, A., Bachmann, J., Buckel, M., Chorbacher, J., and Helten, H. (2026). Merging Pyrrole with Boron into Versatile Di(2-pyrryl)borane Building Blocks: π-Extension, Polymerization, and Coordination. Angew. Chem. Int. Ed. *65*, e16982. https://doi.org/10.1002/anie.202516982.

27. Chang, C., Song, J., Sun, P., Li, C., and Chi, W. (2025). Restriction of Twisted Intramolecular Charge Transfer as a Mechanism for the Aggregation-Induced Emission of Cationic Fluorophores. J. Phys. Chem. A *129*, 7761–7767. https://doi.org/10.1021/acs.jpca.5c02564.

28. Tian, Y., Yin, D., and Yan, L. (2023). J-aggregation strategy of organic dyes for near-infrared bioimaging and fluorescent image-guided phototherapy. WIREs Nanomed. Nanobiotechnol. *15*, e1831. https://doi.org/10.1002/wnan.1831.

29. Insuasty, A., Carrara, S., Xuechen, J., McNeill, C.R., Hogan, C., and Langford, S.J. (2024). Aggregation-Induced Emission of Naphthalene Diimides: Effect of Chain Length on Liquid and Solid-Phase Emissive Properties. Chem. Asian J. *19*, e202400152. https://doi.org/10.1002/asia.202400152.

30. Jelley, E.E. (1936). Spectral absorption and fluorescence of dyes in the molecular state. Nature *138*, 1009–1010. https://doi.org/10.1038/1381009a0.

31. Peng, L., Wei, R., Guo, Y., Zheng, X., Zheng, Y., Ding, Y., Xiang, Y., and Tong, A. (2019). Tuning Emission Wavelength of Polymorphous Crystal via Controllable Alkyl Chain Stacking and Its Vapor- and Thermo-Responsive Fluorescence. Chem. Eur J. *25*, 8043–8052. https://doi.org/10.1002/chem.201900722.

32. Li, E., Jie, K., Liu, M., Sheng, X., Zhu, W., and Huang, F. (2020). Vapochromic crystals: understanding vapochromism from the perspective of crystal engineering. Chem. Soc. Rev. *49*, 1517–1544. https://doi.org/10.1039/c9cs00098d.

33. Wu, K., Yang, R., Song, X., Ju, H., and Liu, Y. (2025). Recent Advances in NIR-II Molecular Aggregates and Applications in the Biomedical Field. Chemosensors *13*, 67. https://doi.org/10.3390/chemosensors13020067.

34. Ma, S., Du, S., Pan, G., Dai, S., Xu, B., and Tian, W. (2021). Organic molecular aggregates: From aggregation structure to emission property. Aggregate *2*, e96. https://doi.org/10.1002/agt2.96.

35. Hua, B., Zhang, C., Zhou, W., Shao, L., Wang, Z., Wang, L., Zhu, H., and Huang, F. (2020). Pillar[5]arene-Based Solid-State Supramolecular Polymers with Suppressed Aggregation-Caused Quenching Effects and Two-Photon Excited Emission. J. Am. Chem. Soc. *142*, 16557–16561. https://doi.org/10.1021/jacs.0c08751.

36. Bera, M.K., Pal, P., and Malik, S. (2020). Solid-state emissive organic chromophores: design, strategy and building blocks. J. Mater. Chem. C Mater. *8*, 788–802. https://doi.org/10.1039/c9tc04239c.

37. Rubert, L., Ehmann, H.M.A., and Soberats, B. (2025). Two-Dimensional Supramolecular Polymorphism in Cyanine H- and J-Aggregates. Angew. Chem. Int. Ed. Engl. *64*, e202415774. https://doi.org/10.1002/anie.202415774.

38. Bricks, J.L., Slominskii, Y.L., Panas, I.D., and Demchenko, A.P. (2017). Fluorescent J-aggregates of cyanine dyes: basic research and applications review. Methods Appl. Fluoresc. *6*, 012001. https://doi.org/10.1088/2050-6120/aa8d0d.

39. Maeda, T., Okamura, N., Das, S., Ishida, T., Kotera, H., Ajayaghosh, A., Saeki, A., and Yagi, S. (2026). Solvent-Controlled Supramolecular Polymerization and Morphology-Depended Photoconductivity Modulation in a Squaraine-Naphthalene Diimide-Squaraine Bulk p/n Heterojunction. Angew. Chem. Int. Ed. Engl. *65*, e16556. https://doi.org/10.1002/anie.202516556.

40. Shen, C.A., and Würthner, F. (2020). NIR-emitting squaraine J-aggregate nanosheets. Chem. Commun. *56*, 9878–9881. https://doi.org/10.1039/d0cc03686b.

41. Hisahara, Y., Nakano, T., and Tamiaki, H. (2025). Effect of the naphthylene linker on the *J*-aggregation abilities of chlorophyll-a derivatives. Photochem. Photobiol. *101*, 1508–1515. https://doi.org/10.1111/php.14076.

42. Hisahara, Y., Nakano, T., and Tamiaki, H. (2023). Self-aggregation behavior of dimeric chlorophyll-a derivatives linked with ethynylene and *m*-phenylene moieties. Photochem. Photobiol. Sci. *22*, 2329–2339. https://doi.org/10.1007/s43630-023-00454-w.

43. Kanno, R., Stolte, M., Stepanenko, V., Pöppler, A.C., Terashima, T., and Würthner, F. (2025). Perylene bisimide J-aggregates in a polymer matrix: controlling self-assembly and fluorescence properties. J. Mater. Chem. C Mater. *13*, 5981–5987. https://doi.org/10.1039/d5tc00409h.

44. Hecht, M., and Würthner, F. (2021). Supramolecularly Engineered J-Aggregates Based on Perylene Bisimide Dyes. Acc. Chem. Res. *54*, 642–653. https://doi.org/10.1021/acs.accounts.0c00590.

45. Jiang, Z., Ma, X., Song, K., Wang, T., Dong, M., Liu, H., Gao, H., Wang, X., Zhao, J., and Liu, Z. (2025). Shortwave infrared absorbing and fluorescent BODIPY J-aggregates for high-contrast imaging. Chem. Sci. *16*, 17779–17792. https://doi.org/10.1039/d5sc03864b.

46. Sun, G., Zhang, Y., Zhou, N., Huo, F., and Yin, C. (2025). Recent advances in the construction, imaging and phototherapy applications of NIR-II J-aggregates based on different fluorophores. Dyes Pigments *243*, 113054. https://doi.org/10.1016/j.dyepig.2025.113054.

47. Brouwer, A.M. (2011). Standards for photoluminescence quantum yield measurements in solution (IUPAC Technical Report). Pure Appl. Chem. *83*, 2213–2228. https://doi.org/10.1351/Pac-Rep-10-09-31.

48. Terenziani, F., Katan, C., Badaeva, E., Tretiak, S., and Blanchard-Desce, M. (2008). Enhanced Two-Photon Absorption of Organic Chromophores: Theoretical and Experimental Assessments. Adv. Mater. *20*, 4641–4678. https://doi.org/10.1002/adma.200800402.

49. Rumi, M., and Perry, J.W. (2010). Two-photon absorption: an overview of measurements and principles. Adv. Opt. Photonics *2*, 451–518. https://doi.org/10.1364/Aop.2.000451.

50. Bruker APEX3 V2019.1 Bruker-AXS, 2019.

51. Sheldrick, G.M. (2015). SHELXT - Integrated space-group and crystal-structure determination. Acta Crystallogr. A Found. Adv. *71*, 3–8. https://doi.org/10.1107/S2053273314026370.

52. Dolomanov, O.V., Bourhis, L.J., Gildea, R.J., Howard, J.A.K., and Puschmann, H. (2009). OLEX2: a complete structure solution, refinement and analysis program. J. Appl. Crystallogr. *42*, 339–341. https://doi.org/10.1107/S0021889808042726.

53. Frisch, M.J., Trucks, G.W., Schlegel, H.B., Scuseria, G.E., Robb, M.A., Cheeseman, J.R., Scalmani, G., Barone, V., Petersson, G.A., Nakatsuji, H., et al. (2016). Gaussian 16 (Rev. C.01).

54. Tomasi, J., Mennucci, B., and Cammi, R. (2005). Quantum mechanical continuum solvation models. Chem. Rev. *105*, 2999–3093. https://doi.org/10.1021/cr9904009.

55. Yanai, T., Tew, D.P., and Handy, N.C. (2004). A new hybrid exchange-correlation functional using the Coulomb-attenuating method (CAM-B3LYP). Chem. Phys. Lett. *393*, 51–57. https://doi.org/10.1016/j.cplett.2004.06.011.

56. Liu, Z., Lu, T., and Chen, Q. (2020). An sp-hybridized all-carboatomic ring, cyclo[18]carbon: Electronic structure, electronic spectrum, and optical nonlinearity. Carbon *165*, 461–467. https://doi.org/10.1016/j.carbon.2020.05.023.

57. Guido, C.A., Cortona, P., Mennucci, B., and Adamo, C. (2013). On the Metric of Charge Transfer Molecular Excitations: A Simple Chemical Descriptor. J. Chem. Theory Comput. *9*, 3118–3126. https://doi.org/10.1021/ct400337e.